

Incompressibility of Impurity Flows in Low Density TJ-II Plasmas and Comparison with Neoclassical Theory

J Arévalo, J A Alonso, K J McCarthy and J L Velasco

Laboratorio Nacional de Fusión, Asociación Euratom-Ciemat, Madrid, Spain

E-mail: juan.arevalo@ciemat.es

Abstract. Poloidal and toroidal velocities of fully-ionised carbon are measured by means of charge exchange recombination spectroscopy (CXRS) in the TJ-II stellarator. We present a detailed treatment of the 3D geometry and show that flow measurements, performed at different locations of the same flux surface, are compatible with flow incompressibility for the low density plasmas under study (line averaged electron densities $\bar{n}_e \leq 10^{19} \text{ m}^{-3}$). Furthermore, comparison with neoclassical calculations shows quantitative agreement with the measured radial electric field and ion bootstrap parallel flow in the absence of an external momentum input.

PACS numbers: 52.30.-q, 52.55.Hc, 52.70.Kz, 52.25.Vy, 52.25.Dg

1. Introduction

Plasma rotation has become one of the key ingredients of fusion plasma performance, after the discovery of a reduction of turbulence and transport [1] through a sheared $E \times B$ rotation. With regard to stability, large toroidal rotations can stabilize resistive wall modes and Neoclassical Tearing modes. For these reasons, the physics of toroidal momentum transport, and the so-called intrinsic rotation, have become a very active area of research, mainly for their importance in the operation of a reactor plasma, for which the external torque will be negligible [2]. Thus, reliable rotation measurements are required. In this sense, the Charge eXchange Recombination Spectroscopy (CXRS) technique [3] has developed into a basic tool for diagnosing plasma rotation over the last three decades, and will be a key diagnostic for ITER [4].

One of the basic results of the kinetic theory of strongly magnetized plasmas with small (compared to thermal) $E \times B$ velocity, is that first order ion and electron flows are parallel to flux surfaces and incompressible [5], *i.e.*, their velocity fields satisfy $\nabla \cdot \mathbf{u} = 0$. This can be understood as a consequence of particle number conservation $\nabla \cdot n\mathbf{u} = 0$ with flux-constant density $n(\rho)$ and zero first-order radial velocity $\mathbf{u} \cdot \nabla \rho = 0$ (here, ρ is a radial coordinate labelling a magnetic surface). Such a velocity field is fully determined by two flux functions (*i.e.*, that depend on spatial coordinates through ρ only). Note that the incompressibility of flows follows from the usual neoclassical (and gyrokinetic) ordering schemes but it neither assumes nor implies the flows to be of 'neoclassical origin'. Indeed, the spatial variation of an incompressible flow has been recently employed to estimate the poloidal velocity from inboard and outboard

toroidal measurements in TCV and DIII-D [6, 7]. Nevertheless, in the Alcator C-Mod [8] and ASDEX-Upgrade [9] tokamaks, it has been observed that as the main ion pressure increases, a significant poloidal variation of the impurity density appears. Indeed, a redistribution of the density of impurities on flux surfaces is expected to be driven by the parallel friction caused by large ion diamagnetic velocities [10], making impurity flows compressible.

There is no clear picture concerning the Neoclassical (NC) nature of poloidal flows in tokamaks. Early measurements on TFTR [11] showed a large discrepancy with the NC theory. However, a deeper understanding of CXRS measurements [12] led to better agreement between experimental poloidal flows and NC expectations on JT-60U, MAST or NSTX (see [13], and references therein), in H-Mode plasmas or even in the presence of an Internal Transport Barrier (ITB). Moreover, recent measurements on Alcator C-Mod [14] and ASDEX-Upgrade [15] have been demonstrated to follow NC theory in the absence of impurity density asymmetries. Nevertheless, poloidal velocity measurements on JET within an ITB [16], and on DIII-D during H-mode and quiescent H-mode [17], are still not fully understood.

On the other hand, toroidal flows in tokamaks are expected to be dominated by mechanisms other than neoclassical, since toroidal viscosity vanishes for axisymmetric systems. Nevertheless, the presence of a sizeable toroidal ripple and/or non-axisymmetric magnetic perturbations for ELM control in tokamak reactors could induce a non-negligible toroidal viscosity. This demands experimental studies on rotation in stellarator devices, since in such machines plasma cannot rotate freely [18], and the radial electric field is determined by the ambipolarity condition on the NC radial particle fluxes. Detailed comparisons of the NC radial electric field with CXRS measurements have been performed on the W7-AS stellarator, showing reasonable agreement for most of the plasma scenarios studied [19]. In addition, in the LHD and CHS stellarators, qualitative agreement was found between radial electric field measurements and calculations with simplified NC theories [20, 21]. The effect of the magnetic field ripple on the toroidal flows was also investigated in CHS [22] and LHD [23], showing qualitative effects of helical and toroidal ripple on spontaneous toroidal flow. Finally, a recent work in HSX has shown a clear discrepancy between the experimental and NC radial electric fields [24]. The authors claim that the monoenergetic approximation used by DKES might be inadequate for radial electric fields close to the helical resonance. Nonetheless, the parallel flow was well reproduced after including momentum-correction techniques and impurities in the calculations.

In the TJ-II stellarator [25], the radial electric field has been studied by means of the Heavy Ion Beam Probe (HIBP) [26] and Doppler Reflectometry [27] diagnostics. Measurements from the former showed consistency with NC calculations in the electron root, within a factor a two [26]. However, the experimental values systematically exceed the NC predictions in the ion-root operation [28]. In addition, passive spectroscopy has been utilized to measured poloidal and toroidal rotations of impurities [29, 30]. Qualitative agreement was reported between the experimental poloidal flow and NC values, mainly in the change of root as density increases [31]. In contrast, significant discrepancies were found in the toroidal flows for the different species studied and with NC calculations [30].

In this work we use CXRS to measure fully ionized carbon impurity flows in low density plasmas of the TJ-II stellarator and compare them with neoclassical calculations. First, we present in section 2 the diagnostic technique, together with a general treatment of the sightlines and flow geometry, which allows the extraction

of the two flux-surface averaged (FSA) flows from two velocity measurements. These flux constants define an incompressible flow within a flux surface and are related to the radial electric field and the bootstrap velocity. In section 3.1, the method is applied to two pairs from three measurements (poloidal, outboard-toroidal and inboard-toroidal) to show that the spatial variation of the flow is consistent with incompressibility. Finally, the measured flows are compared with neoclassical predictions (Section 3.2) and good agreement is found for the radial electric field (in all the cases studied) and bootstrap flows (in ECRH plasmas without momentum injection).

2. Experimental set-up and data analysis

The TJ-II is a four-period heliac-type stellarator with major radius of $R_0 = 1.5$ m and averaged minor radius of $a \leq 0.22$ m [25]. Hydrogen plasmas are created and heated by 2 gyrotrons operated at 53.2 GHz ($P_{ECRH} \leq 600$ kW). During this heating phase central electron densities, $n_e(0)$, and temperatures, $T_e(0)$, up to $1.7 \times 10^{19} \text{ m}^{-3}$ and 1 keV, respectively, are achieved. In addition, plasmas can be maintained by two tangential Neutral Beam Injectors (NBI), each providing ≤ 500 kW. As a result, plasmas with $n_e(0) \leq 5 \times 10^{19} \text{ m}^{-3}$ and $T_e(0) \leq 400$ eV are attained. The machine is operated with lithium wall coating, which allows density control, but results in a strong reduction in impurity concentrations and hence in impurity photon emission fluxes. In order to undertake CXRS measurements in such conditions, a high-throughput optical system and spectrograph, plus a high-efficiency detector, are needed [32]. These are described next.

The CXRS process of interest in TJ-II involves electron capture from accelerated hydrogen by fully ionized carbon ions into a highly excited state of C^{5+} , followed by spontaneous decay via photon emission, *i.e.* the C VI line at 529.07 nm ($n = 8 \rightarrow 7$). For this, a compact Diagnostic Neutral Beam Injector (DNBI) provides a 5 ms long pulse of neutral hydrogen accelerated to 30 keV (the ratio of its full, half and third energy components is 90 : 8 : 2) [32]. Its $1/e$ -radius at focus is 21 mm.

For light collection, a bidirectional optical system, consisting of commercial camera lenses and 12-way fibre optic bundles, collects the C^{5+} light across the outer half of the plasma diameter with ~ 1 cm spatial separation between lines of sight. These components are installed in top and bottom access ports located in the same machine sector as the DNBI. A second optical system with a 16-way fibre bundle, (12 equally spaced fibres along a row plus four additional fibres that straddle the row on both sides), views almost the complete beam/plasma interaction volume from a nearby tangential viewing access port. This provides ~ 3.4 cm spatial separation between sightlines. Note: a retractable in-vacuum mirror located in the mouth of the access port is needed to redirect light to the lens as the port is shared with a neutral particle analyser diagnostic.

A schematic layout of the diagnostic sightlines is depicted in figure 1. As observed, poloidal cuts of TJ-II magnetic surfaces are bean shaped and exhibit large flux compressions within a surface. The plasma minor radius region scanned by nearly symmetric poloidal views is $\rho \in (0.25, 0.85)$ in the standard magnetic configuration, 100_44.64 (where the nomenclature reflects currents in the central, helical and vertical field coils, respectively). Here, a normalised radius $\rho \equiv \sqrt{V/V_0}$ is defined, where V and V_0 are the volumes enclosed by the surface of interest and the last closed magnetic surface, respectively. As explained in section 2.2, poloidal top fibres are used to correct for uncertainties in the C^{5+} rest emission wavelength, and thus, do

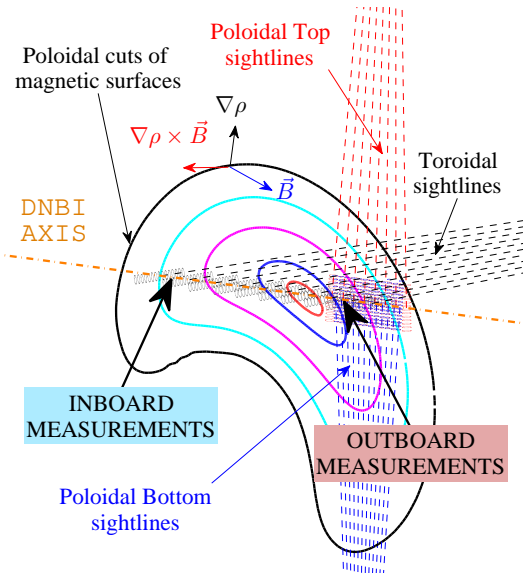


Figure 1. Schematic diagram of CXRS diagnostic sightlines for the standard magnetic configuration. Only 8 Poloidal Top lines of sight are shown, as the outboard 4 do not provide useful data for this configuration. Inboard and outboard toroidal measurements are highlighted. In addition, poloidal cuts of magnetic surfaces are presented, together with the directions of concern for velocity measurements: radial ($\nabla\rho$), parallel (\mathbf{B}) and $\nabla\rho \times \mathbf{B}$. Note that none of these vectors is contained in the poloidal plane. The magnetic field vector, \mathbf{B} , points into the page.

not provide additional information about the C^{6+} distribution function. On the other hand, the toroidal fibres cover both sides of the magnetic axis, from $\rho = -0.7$ to $\rho = 0.6$ at 10 locations (2 of the 12 sightlines are obstructed by the vacuum chamber). The region in which both poloidal and toroidal measurements are taken is labelled as outboard, in analogy with tokamaks; while the zone where only toroidal measurements are made is labelled as inboard. The nomenclature $\rho \geq 0$ and $\rho \leq 0$ is also utilized to define these regions. In the outboard region, poloidal and toroidal fibres view the same surfaces at $\rho \sim 0.2, 0.4$ and 0.6 . Therefore, the 2D-flow velocity is completely determined at these locations. The redundant inboard-toroidal measurements will be used in section 3.1 to verify whether the incompressibility assumption holds or not.

Light collected by all systems is transferred to the input of a light dispersion element, an holographic imaging spectrograph, modified with three $100 \mu\text{m}$ -wide curved entrance slits (to compensate for the short focal length) and equipped with a transmission grating sandwiched between two BK7 prisms. It provides a focal-plane dispersion of $\sim 1.15 \text{ nm/mm}$ at 529 nm [32]. In addition, a narrow bandpass filter ($2.0 \pm 0.5 \text{ nm}$ at full-width at half-maximum) prevents spectral overlapping of the light from the three fibre arrays at the image plane. The set-up also includes a high-efficiency back-illuminated CCD camera and a fast mechanical shutter ($\geq 4.5 \text{ ms}$ time window). Using on-chip binning, multiple spectra are collected during discharges ($\leq 300 \text{ ms}$).

In order to obtain neutral beam induced spectral line data, and hence spatially localized information, it is necessary to remove background -passive- C^{5+} light

from spectra. This is done by alternatively injecting and not injecting the DNBI into reproducible plasmas (shot-to-shot technique) [32]). Then, by subtracting a background spectrum from the stimulated plus background -active plus passive-spectrum the CXRS data is obtained. For ECRH plasmas, the active emission is a factor of ~ 5 smaller than the passive one, see figure 2. In NBI heated plasmas, this ratio is reduced to a factor of 2. A multi-Gaussian fit to the active signal is also shown, and will be explained in Section 2.2.

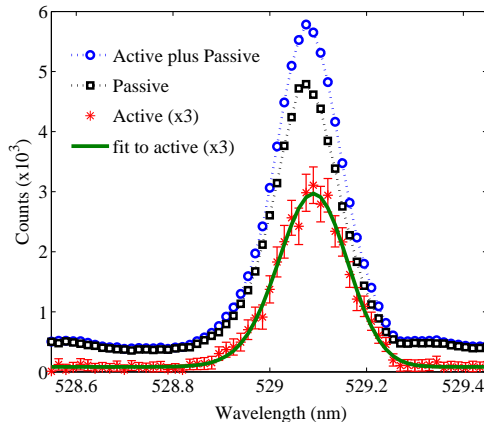


Figure 2. DNBI-excited raw C-VI spectral line data (Active plus Passive) and background emission (Passive), for two reproducible ECRH discharges. The active signal is obtained from the difference. A multi-Gaussian fit to the latter is presented.

Correctly performed instrumental wavelength calibration and correction are essential if experimental uncertainties are to be minimized. Indeed, wavelength calibration is done regularly during TJ-II operation, as thermal variations in the instrument can be significant, *e.g.*, $4 \mu\text{m K}^{-1}$ at the focal plane, this being equivalent to an offset of $\sim 2.6 \text{ km s}^{-1} \text{ K}^{-1}$. For this, spectral lines from a neon pencil-type lamp are used to establish the wavelength dispersion at each fibre location on the focal plane [32]. Finally, several well-studied effects are negligible for TJ-II or require correction before the Doppler shift of the beam induced C VI spectral lines can be determined. These effects, together with machine specific effects such as magnetic geometry and beam/sightline volumes, are handled by an in-house software package developed to analyse the data and obtain impurity ion temperature and velocities. These are described in more detail in Section 2.2.

2.1. Optical alignment

Alignment of the bidirectional poloidal sightlines is performed by illuminating each fibre bundle with an intense light source and observing, through a nearby view-port, the orientation and location of the resultant bright spots with respect to markings on the inside of the opposing vacuum flange. From these, the sightline paths through the neutral beam can be determined using a cross-sectional machine drawing and magnetic configuration maps.

On the other hand, alignment of the tangential viewing sightlines involves aligning the in-vacuum mirror as well as orienting the fibre bundle ferrule. For this, a

preliminary alignment is made by illuminating the fibres with the intense light source and observing, through a view-port located in a sector downstream of the neutral beam sector, the location of bright spots on the inside of the vacuum chamber. Then, after removing the light source, the fibre ends that attach to the spectrograph input fibre bundle, are connected to Avalanche Photodiodes (APD) whose bias voltages were previously adjusted to a common gain. Then, by repeatedly injecting the DNBI into the TJ-II chamber, the mirror and fibre bundle are adjusted in-turn until all APD signals are maximized. Moreover, as an additional check, light from the sightlines that straddle the 12 principal sightlines are checked for symmetry about the beam centre. Finally, by repeating the fibre illumination procedure described before for the toroidal fibres, the location of bright spots on the vessel inboard wall are noted and cross-checked. Then, using a 3 dimensional computer aided design (CAD) software with the geometrical coordinates of the vacuum chamber, neutral beam and sightlines as inputs, the beam/sightline crossing points are found for the magnetic configuration of interest.

2.2. Carbon impurity temperature, density and velocity measurements

In figure 2, a multi-Gaussian fit to an active signal obtained with the shot-to-shot technique is made using the expression:

$$I_C = I_0 \sum_j a_j \exp \left\{ - \left(\frac{\lambda - \delta\lambda_j - \lambda_c}{\sigma} \right)^2 \right\}, \quad (1)$$

where a_j is the relative amplitude of each of the fine structure components of the C^{5+} spectral line when assuming a statistical population of the initial j -levels, and normalized to the sum, $\sum_j a_j = 1$. $\delta\lambda_j$ stands for the wavelength separation of the fine-structure components respect to the rest wavelength: $\lambda_0 = \sum_j a_j \lambda_j = 5292.04 \text{ \AA}$ in vacuum [33]. In addition, λ_c measures the line centroid. Carbon temperatures are obtained from the parameter σ , after considering Zeeman broadening and a numerical deconvolution of the instrumental function [34]. A representative temperature profile of the ECRH phase is displayed in figure 3. It is found that CXRS temperature measurements from the three fibre arrays coincide, within error bars, on both sides of the magnetic axis. Indeed, the consistency of the temperature measurements from the three fibre arrays is used usually as an additional check of the diagnostic optical alignment. For completeness, the majority ion temperature measured at $\rho \sim 0$ by the poloidal Neutral Particle Analyser (NPA), is shown.

Carbon impurity density measurements are more challenging, since the beam density, n_b , needs to be known. The latter can be roughly estimated by considering a simple pencil-like beam attenuation model [35], together with analytical expression to account for the beam profile in vacuum. Besides, the optical system is not absolutely calibrated at present. However, an estimate can be made by assuming that the relative efficiency of each fibre is proportional to the total intensity recorded during the instrument calibration procedure, *i.e.*,

$$\langle n_{C^{6+}} \rangle_{\mathcal{V}_{\text{los}}} \propto \frac{1}{\int_{\mathcal{V}_{\text{los}}} d^3\mathbf{r} n_b} \frac{\int d\lambda I_C}{\int d\lambda I_{Ne}}, \quad (2)$$

where the integral of the beam atoms is performed in the sightlines measurement volume, \mathcal{V}_{los} .

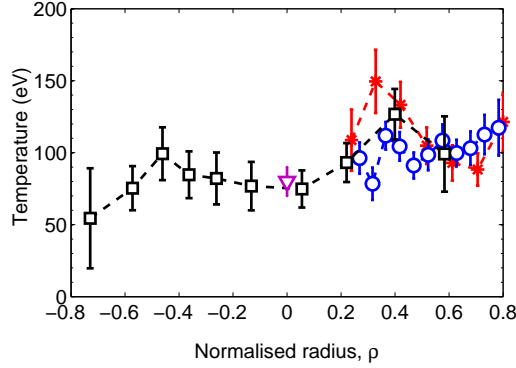


Figure 3. Fully-ionized carbon ion temperature profile for a representative ECRH discharge (discharge #25801, with $n_e(0) \approx 0.5 \times 10^{19} \text{ m}^{-3}$ and $T_e(0) \approx 0.8 \text{ keV}$), as measured by poloidal top (blue circles), bottom (red asterisks) and toroidal sightlines (black squares). The central majority ion temperature measured by the NPA is shown as well (triangles).

Finally, the velocity along sightlines, $v_l = \vec{v} \cdot \hat{e}_l$, is obtained from the line centroid shift, λ_c :

$$\lambda_c = (\lambda_0 + \lambda_{cx}) \left(1 + \frac{v_l}{c} \right) \approx \lambda_0 \left(1 + \frac{v_l}{c} \right) + \lambda_{cx}. \quad (3)$$

Here, λ_{cx} accounts for possible deviations in the populations of the fine structure level from a complete statistical mixing, that might cause a false velocity. This is removed by adding the redundant measured wavelengths from top and bottom poloidal sightlines, since they are almost symmetrically opposite.

It is well documented that the daughter distribution function of C^{5+} ions may exhibit some undesired velocities, usually named *pseudo-velocities*, which arise from the energy dependence of the beam/carbon charge exchange cross-section as well as the gyromotion of the impurity during the de-excitation process [12]. In TJ-II, due to the relatively small magnetic field strength and temperatures, the only significant contribution comes from the former, which is orientated in the DNBI direction. These effects are only substantial for the toroidal view (since the poloidal sightlines view the beam almost perpendicularly), being of the order of $\sim 1 - 2 \text{ km s}^{-1}$, at most.

2.3. Data Analysis

The general form of the impurity velocity field is [5]:

$$\mathbf{u} = E(\rho) \frac{\mathbf{B} \times \nabla \rho}{B^2} + \left(\frac{\langle \mathbf{u} \cdot \mathbf{B} \rangle}{\langle B^2 \rangle} + E(\rho)h \right) \mathbf{B}, \quad (4)$$

where the perpendicular velocity is given by $\mathbf{E} \times \mathbf{B}$ and diamagnetic contributions, and thus,

$$E(\rho) = \frac{d\Phi}{d\rho} + \frac{1}{nZe} \frac{dp}{d\rho}. \quad (5)$$

Here, n , (Ze) and p are the density, charge and pressure of the impurity, respectively. In addition, Φ is the electric potential and $\langle \cdot \rangle$ denotes flux-surface average. The last

term in equation (4) is the well-know Pfirsch-Schlüter (PS) flow, which arises from the toroidicity of the magnetic field strength, and satisfies:

$$\mathbf{B} \cdot \nabla h = -\mathbf{B} \times \nabla \rho \cdot \nabla \left(\frac{1}{B^2} \right), \quad \langle hB \rangle = 0. \quad (6)$$

In order to obtain flux-surface averaged (FSA) flows from poloidal and toroidal velocity measurements, it is convenient to define dimensionless vectors, which store the variation of the flow within the surface. These are:

$$\mathbf{f} = -\frac{\langle B \rangle}{\langle |\nabla \rho| \rangle} \left(\frac{\mathbf{B} \times \nabla \rho}{B^2} + h\mathbf{B} \right), \quad (7)$$

$$\mathbf{g} = \frac{\langle B \rangle}{\langle B^2 \rangle} \mathbf{B}. \quad (8)$$

Note that the vector \mathbf{f} has both perpendicular and parallel components, the latter coming from the PS contribution: $\mathbf{f} \equiv \mathbf{f}_\perp + \mathbf{f}_{\text{PS}}$. Then, impurity flows are expressed as:

$$\mathbf{u} = \mathbf{f}U_\perp(\rho) + \mathbf{g}U_b(\rho). \quad (9)$$

Here, the following perpendicular and parallel FSA flows are defined:

$$U_\perp(\rho) \equiv \frac{E_r}{\langle B \rangle} - \frac{1}{nZe} \frac{dp}{d\rho} \frac{\langle |\nabla \rho| \rangle}{\langle B \rangle}, \quad (10)$$

$$U_b(\rho) \equiv \frac{\langle \mathbf{u} \cdot \mathbf{B} \rangle}{\langle B \rangle}, \quad (11)$$

where the FSA radial electric field is given by: $E_r(\rho) \equiv -\langle |\nabla \rho| \rangle d\Phi/d\rho$.

Finally, taking the projections of the velocity vector \mathbf{u} over the poloidal-bottom and toroidal sightlines ($u_p = \mathbf{u} \cdot \hat{e}_p$ and $u_t = \mathbf{u} \cdot \hat{e}_t$, respectively) the FSA mean velocities are obtained from the measured flows:

$$\begin{pmatrix} U_\perp(\rho) \\ U_b(\rho) \end{pmatrix} = \frac{1}{\Delta} \begin{pmatrix} g_t & -g_p \\ -f_t & f_p \end{pmatrix} \begin{pmatrix} u_p \\ u_t \end{pmatrix}. \quad (12)$$

Here, $\Delta = g_t f_p - g_p f_t$, and the sub-index (p, t) denote the projection of a vector (\mathbf{u} , \mathbf{g} or \mathbf{f}) over the poloidal and toroidal lines of sight. Accordingly, the FSA flows can be obtained from two different measurements performed on a surface, but not necessarily at the same location. The results of this procedure are presented in the next section.

The projection of the geometrical vectors, \mathbf{f} or \mathbf{g} , over the poloidal-bottom and toroidal sightlines is depicted in figure 4. The vector \mathbf{f} has been split into their parallel and perpendicular components, to illustrate their contributions on the velocity field. As expected, the poloidal velocity is dominated by the perpendicular contribution, although the parallel one (through the $\mathbf{g} \cdot \hat{e}_p$ factor) has to be accounted for. The sample volumes located at the outboard are close to stagnation points of the PS flow and therefore its contribution to these measurements is modest, unlike in the inboard region where it can become dominant for toroidal velocities. In addition, the mean values of a geometrical quantity, $X(\mathbf{r})$, have been obtained through an average over the measurement volume for a given fibre, \mathcal{V}_{los} :

$$\langle X \rangle_{\mathcal{V}_{\text{los}}} = \frac{\int_{\mathcal{V}_{\text{los}}} d^3 \mathbf{r} n_b n_e X(\mathbf{r})}{\int_{\mathcal{V}_{\text{los}}} d^3 \mathbf{r} n_b n_e}, \quad (13)$$

Note that the integral should be weighted with the local carbon impurity density, rather than the electron density. Although the former is missing, we consider this

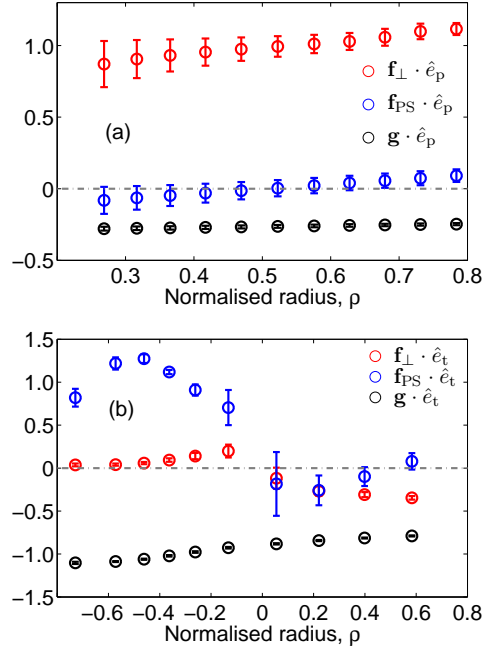


Figure 4. Dimensionless factors that store the variation of the flows on the surface for the (a) poloidal-bottom and (b) toroidal fibre arrays. The vector \mathbf{f} has been split into their parallel and perpendicular components ($\mathbf{f}_{PS} = \mathbf{f} \cdot \hat{\mathbf{b}}$ and $\mathbf{f}_\perp = (\hat{\mathbf{b}} \times \mathbf{f}) \times \hat{\mathbf{b}}$, respectively).

approximation sufficiently good to obtain mean values. The errors associated with geometrical quantities, ε_X , are given by its standard deviation in the measurement volume: $\varepsilon_X^2 = \langle X^2 \rangle_{V_{los}} - (\langle X \rangle_{V_{los}})^2$, and are propagated through the code. It can be observed that when moving towards the plasma centre, the dispersion in these factors increases, since the poloidal views become more perpendicular to the surfaces. The errors in the results will consist of the statistical ones, plus those due to the average in the measurement volume.

3. Results

In this work, two plasmas scenarios are considered, both being operated in the standard magnetic configuration. The first one, heated by ECRH, is characterized by flat electron density ($n_e(0) \approx 0.5 \times 10^{19} \text{ m}^{-3}$) and peaked electron temperature profiles ($T_e(0) \approx 0.8 \text{ keV}$), see figure 5. However, ions remain cooler, $T_i(0) \sim 80 \text{ eV}$ ($T_i \approx T_c$ is assumed, see the comparison in figure 3), with slightly hollow temperature and impurity density profiles. The data presented here corresponds to TJ-II discharge #25801, which is representative of several similar discharges that are briefly discussed at the end of this section.

In the second scenario, plasmas are heated with a tangential NBI injected in the direction of the toroidal magnetic field. The resultant density profile is more peaked, with $n_e(0) \approx 1.6 \times 10^{19} \text{ m}^{-3}$, whilst the electron temperature decreases to $T_e(0) \sim 300 \text{ eV}$. In contrast, the ion channel reaches temperatures up to 200 eV. The discharge

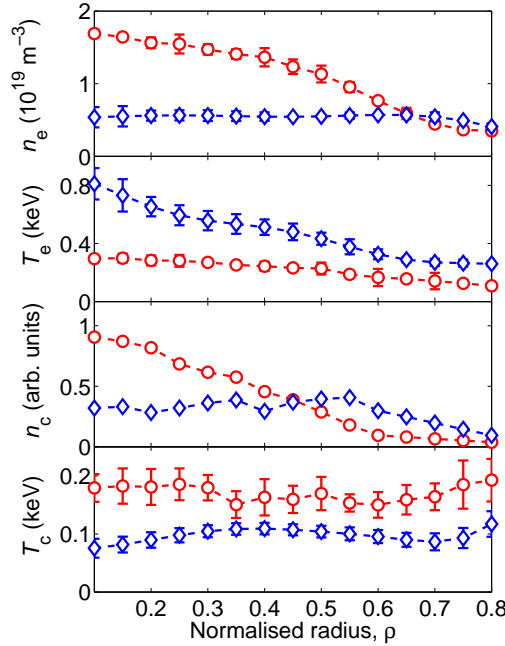


Figure 5. Profiles of n_e , T_e , n_c and T_c (from top to bottom) for the ECRH scenario, shot #25801 (blue diamonds); and the NBI case, discharge #28263 (red circles).

chosen for this case, #28263, is not representative of fully developed NBI heated plasmas, as it corresponds to the first steps of the NBI phase, where the density grows rapidly. Nevertheless, it is included in this paper to highlight that for these low density plasmas the results are independent of the heating method.

Finally, the measurements presented are restricted to the region $|\rho| \leq 0.8$, because CXRS measurements are not reliable at the edge of TJ-II, due to the poor statistics and the possible presence of suprathermal ions [36].

3.1. Flow incompressibility

The assumption of an incompressible velocity field like the one in equation (4) is widely used in present day CXRS data analysis. In this subsection we verify this by applying the method developed in the previous section, equation (12), to the poloidal and toroidal velocities measured in the discharges presented in figure 5.

The observed velocity pattern, after correcting for fine structure effects and pseudo-velocities, is represented in figure 6 for the ECRH and NBI heating scenarios under study. Poloidal top velocity measurements are not shown, since they were already used to correct for fine structure effects, and so do not provide further information about poloidal flow. In this figure, positive velocities corresponds to particles moving away from the observer. In the ECRH plasma, the toroidal rotation is opposite to the magnetic field direction, while the toroidal flow is reversed in the NBI case. In addition, ECRH toroidal measurements exhibit a strong in/out asymmetry that is explained next.

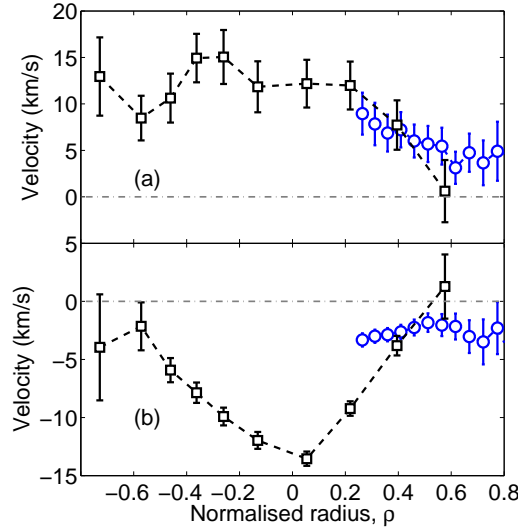


Figure 6. Carbon impurity ion flows observed by toroidal (black squares) and poloidal bottom (blue circles) sightlines, for the: (a) ECRH plasma, discharge #25801; and (b) NBI plasma, discharge #28263.

As commented before, CXRS toroidal velocity measurements are performed on both sides of the magnetic axis in TJ-II. Therefore, they are suitable for the verification of flow incompressibility, due to its redundancy on several magnetic surfaces. In figure 7 the perpendicular, $U_{\perp}(\rho)$, and parallel, $U_{\parallel}(\rho)$, FSA flows obtained are plotted. The values that result from inboard toroidal measurements are presented as open circles, whilst the ones deduced from outboard toroidal velocities are squares. In both cases, the poloidal measurements inserted in equation (12) come from the outboard region.

The agreement found between inboard/outboard measurements confirms the main hypothesis of the applied method, *i.e.*, that impurity flows are incompressible for the low density plasmas presented here. Indeed, to the authors' knowledge, this is the first time that this fundamental assumption of kinetic theory is checked with independent measurements at different locations of a surface (recent work at TCV and DIII-D [6, 7] extract the poloidal flow from toroidal in/out measurements, but are not compared with direct poloidal measurements, due to difficulties associated with such measurement in these tokamaks).

The strong asymmetry in the toroidal velocity observed in the ECRH scenario, figure 6 (a), is explained by the larger -compared to the NBI case- perpendicular flow, which generates significant variations in the parallel velocity, through the local Pfirsch-Schlüter flow. As expected, there is a change from electron to ion root in the radial electric field with increasing density [31], and therefore, a change of sign in U_{\perp} (the impurity diamagnetic contribution is negligible, except for $\rho \sim 0.7$ in the NBI case, where it reaches $\sim 1 \text{ km s}^{-1}$). Finally, a positive parallel velocity is observed in the NBI plasmas, which is compatible with the injection of the beam in the direction of the magnetic field. This will be discussed in the next subsection.

As an indication of the importance of this previous check on the flow spatial variation prior to its comparison with neoclassical estimates, we note that in higher

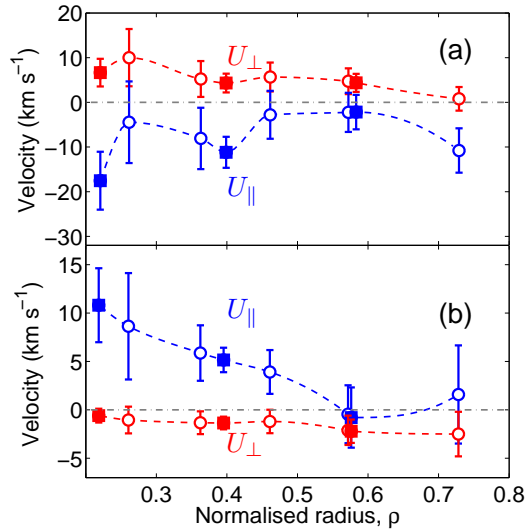


Figure 7. Flux-surface averaged flows $U_{\perp}(\rho)$ and $U_{\parallel}(\rho)$, for the: (a) ECRH discharge, #25801; and (b) NBI plasma, #28263. The circles correspond to toroidal measurements performed in the inboard region, and the squares to those taken in the outboard one.

density NBI plasmas a *compressible* flow variation is observed in TJ-II. This makes the comparison of parallel velocities with standard neoclassical theory not straightforward. Indeed, impurity density variations within a flux surface have been theoretically predicted in the presence of large ion pressure gradients [10], and recently observed in several tokamak devices (Alcator C-Mod [8] and ASDEX-Upgrade [9]). The asymmetry is related to ion-impurity friction and ultimately to impurity radial fluxes, which makes its comprehension particularly relevant for nuclear fusion. The analysis of such plasmas will be presented in a subsequent article.

3.2. Comparison with Neoclassical theory

The Drift Kinetic Equation is solved by using the numerical code DKES [37] complemented with momentum correction techniques. DKES allows to calculate the monoenergetic transport coefficients of the magnetic configuration. These coefficients are convoluted with a Maxwellian distribution function which in turn depends on local density and temperature. Inclusion of the thermodynamical forces (gradients of density and temperature and radial electric field) allows the FSA neoclassical fluxes to be estimated. The neoclassical radial electric field itself is found iteratively by imposing ambipolarity on the particle radial fluxes. Specific details of the procedure are found in [38, 39].

The inputs for this calculation are the magnetic field equilibrium and TJ-II density and temperature profiles. The former is taken to be the vacuum equilibrium, for the low β plasmas studied here. The latter require integration of data from the Thomson Scattering, Helium beam probe, Reflectometry, Interferometry (see [40] and references there in) and CXRS diagnostics. The uncertainties in the transport coefficients and in the measured profiles are propagated to the final theoretical estimate, as in [38].

In order to estimate accurately the parallel and poloidal momentum balance, one should make the calculation by including protons, electrons and main impurities present in the plasma. However, for the lithium-coated plasmas studied in this work, the impurity concentration is low [25] and does not modify the poloidal momentum balance, leaving E_r unchanged. Since the impurity diamagnetic term is small, this completely determines the poloidal impurity rotation. On the other hand, once one ensures momentum conservation in the calculations (by including interspecies friction), the bootstrap flow of the trace impurities is shown to follow that of the bulk ions, which are calculated as in [38]. Finally, one may wonder if values of E_r close to resonances could be found, as in [24]. In such a case, the poloidal $E \times B$ and magnetic drifts cancel out, producing a peaking of the radial fluxes, and the local ansatz underlying DKES computations fails. At TJ-II, this happens for very large values of E_r [41]. The agreement found in the present comparison supports the hypothesis in our calculation.

Some general considerations can be made, following the results obtained for model plasma profiles [38, 39]. Low density ECRH plasmas in TJ-II are in the electron root: E_r is positive and large, and therefore it partially cancels the large contribution of the T_e gradient to the electron radial transport (see figure 5). This large radial electric field drives a large ion parallel flow, especially close to the centre, where the fraction of trapped particles is small and E_r is considerable. On the contrary, NBI plasmas are in the ion root. In order to reduce the ion particle radial transport, driven by the ion temperature gradients, to the electron level, E_r is small and negative. This partial cancellation of the ion channel has consequences in the parallel momentum balance as well, where the negative E_r leads to a small ion bootstrap current.

In the following, the results of a comparison between NC theory and CXRS measurements are presented. Since CXRS active data has been obtained from two different discharges (shot-to-shot technique), we compare the experimental data with the average of NC outcomes for both plasmas.

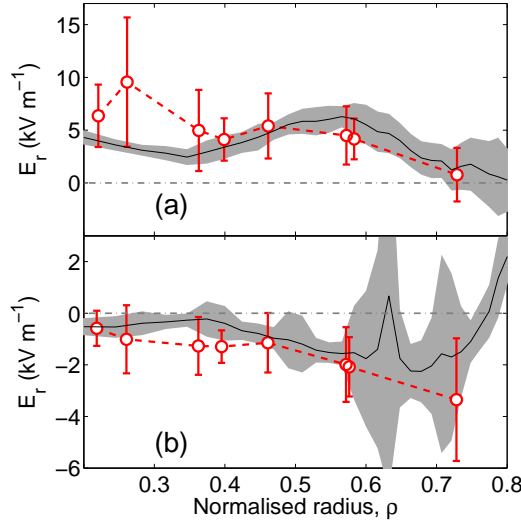


Figure 8. Comparison of Neoclassical (grey shading) and measured (red circles) E_r , for the: (a) ECRH discharge, #25801; and (b) NBI plasma, #28263.

In figure 8, the measured and calculated radial electric field are shown. The experimental values are in agreement with previous results obtained in similar plasmas with the HIBP diagnostic [26], and agree with the NC predictions agree within the error bars. Nonetheless, the mean values observed at the core of the ECRH plasma are somewhat larger than that of the neoclassical estimate; however, the error bars are large. Moreover, the contribution to the experimental E_r from toroidal measurements, $\propto -f_{\parallel} \hat{b} \cdot \hat{e}_{bot} u_t$, equation (12), is similar to that of the poloidal flows, $\propto f_{\parallel} \hat{b} \cdot \hat{e}_{tor} u_p$, due to the high toroidal velocities observed in the core region, see figures 4 and 6 (a). This increases the uncertainties in E_r , since toroidal sightlines are almost aligned with the magnetic field lines, and thus, the extraction of its perpendicular contribution is less reliable.

In the NBI plasma, the experimental errors are reduced, see figure 8 (b). The inferred radial electric field is in good quantitative agreement with neoclassical calculations. The error bars about the NC estimates in figure 8 correspond to dispersion in the ambipolar condition when one considers the not insignificant uncertainties in the plasma profiles, as in [39]. In particular, for $\rho \geq 0.6$, both electron and ion roots can result, as different values of density and temperature are considered within the error bars of figure 5, hence the large uncertainties. Finally, the agreement found for this discharge in the radial electric field suggests that fast NBI ions do not contribute significantly to the radial ambipolar balance, although they inject parallel momentum, as discussed in the following text.

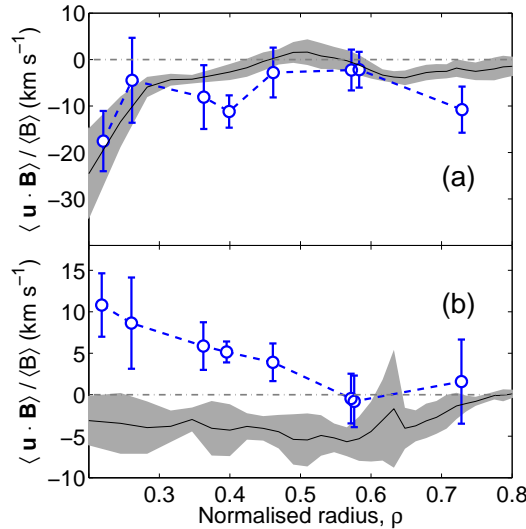


Figure 9. Comparison of Neoclassical and measured parallel flow, U_b , for the: (a) ECRH discharge, #25801; and (b) NBI plasma, #28263.

Figure 9 (a) shows calculations of neoclassical bootstrap ion flow during the ECRH phase, together with the C^{6+} parallel flux-surface flow, $\langle \mathbf{u} \cdot \mathbf{B} \rangle / \langle B \rangle$. A strong parallel rotation driven by the radial electric field is observed at the core region, that is well reproduced by the neoclassical predictions. In the higher density unbalanced NBI case, the parallel flow consists of the neoclassical one (bootstrap), plus the rotation induced by the injected neutrals. Indeed, these measurements show that the latter dominates,

being able to reverse sign. Since this is a low density NBI plasma, the injected fast neutrals can penetrate into the core. This would explain why the deviation of the parallel flow is maximum towards $\rho \sim 0.2$, whilst measured parallel flow approaches bootstrap calculations for $\rho \geq 0.6$.

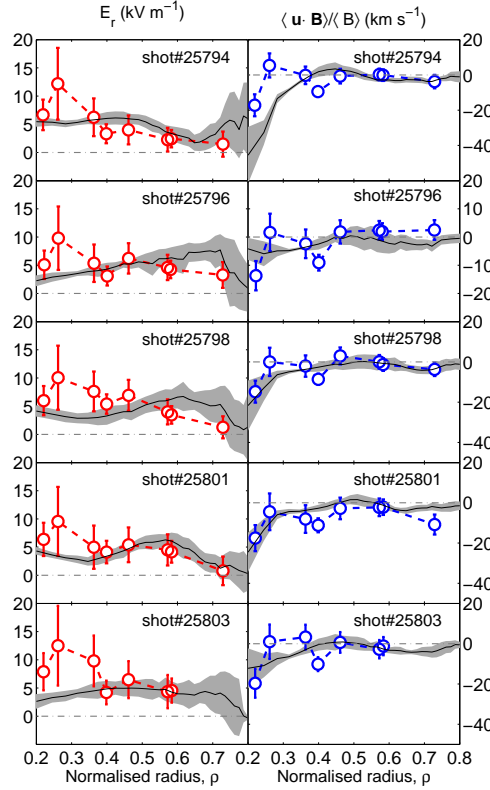


Figure 10. Comparison of NC and measured radial electric field and bootstrap flow, for a set of ECRH discharges. Circles correspond to CXRS measurements, and grey shading to NC estimates.

Finally, to highlight the reproducibility of the results in the ECRH scenario, the comparison of the measured radial electric field and bootstrap flow with NC calculations have been depicted in figure 10, for a set of similar ECRH discharges. The features observed in figures 8 (a) and 9 (a) are replicated in these discharges, and the agreement with the NC calculations is repeated as well.

4. Conclusion

In summary, a comparison between CXRS carbon impurity flow measurements and NC calculations has been done. In addition, the basic form of the velocity field, *i.e.* a divergence-free flow tangent to magnetic surfaces, has been verified. To this end, a general treatment of sightlines and flow geometry has been applied to two pairs of three independent velocity measurements performed at different locations of a flux surface, and consistency with a 2D incompressible flow has been demonstrated.

In addition, good quantitative agreement has been found between measured and NC radial electric fields for low density ECRH plasmas. Furthermore, a comparison of impurity parallel rotation with NC bootstrap flow has been done for the first time in TJ-II, showing consistency with the calculations in these plasmas. In an unbalanced NBI discharge with relatively low density, a similarly good agreement has been found for the radial electric field, while a change in the direction of parallel rotation (with respect to the NC calculations, which do not account for momentum injection) has been observed. This points to a minor role of the fast ion-driven radial current in the ambipolar balance (or poloidal momentum balance) of the TJ-II stellarator.

Acknowledgement

The authors are indebted to the TJ-II experimental group. They would like to thank B. Zurro for useful discussions, and C. Hidalgo for his support. J. Arévalo acknowledges financial support from the FPI grant awarded by CIEMAT (BOE resolution n 171, 24/06/2008).

References

- [1] Terry P.W. 2000 *Rev. Mod. Phys.* **72** 109
- [2] Doyle E.J. *et al* 2007 *Nucl. Fusion* **47** S18; Hender T.C. *et al* 2007 *Nucl. Fusion* **47** S128
- [3] Isler R.C. 1994 *Plasma Phys. Control. Fusion* **36** 171
- [4] Donné A.J.H. *et al* 2007 *Nucl. Fusion* **47** S337
- [5] Hinton F.L. and Hazeltine R.D. 1976 *Rev. Mod. Phys.* **48** 239
- [6] Camenen Y. *et al* 2012 *EPS Conf. on Plasma Phys., Stockholm (Sweden)*.
URL: <http://ocs.ciemat.es/epsicpp2012pap/pdf/O5.117.pdf>
- [7] Chrystal C. *et al* 2012 *Rev. Sci. Instrum.* **83** 10D501
- [8] Marr K D *et al* 2010 *Plasma Phys. Control. Fusion* **52** 055010
- [9] Pütterich T. *et al* 2012 *Nucl. Fusion* **52** 083013
- [10] Helander P. 1998 *Phys. Plasmas* **5** 3999
- [11] Bell R.E. *et al* 1998 *Phys. Rev. Lett.* **81** 1429
- [12] Bell R.E. and Synakowski E.J. 2000 *AIP Conf. Proc.* **547** 39
- [13] Bell R.E. *et al* 2010 *Phys. Plasmas* **17** 082507
- [14] Kagan G. *et al* 2011 *Plasma Phys. Control. Fusion* **53** 025008
- [15] Viezzer E. *et al* 2012 *EPS Conf. on Plasma Phys., Stockholm (Sweden)*.
URL: <http://ocs.ciemat.es/epsicpp2012pap/pdf/O5.118.pdf>
- [16] Tala T. *et al* 2007 *Nucl. Fusion* **47** 1012
- [17] Solomon W.M. *et al* 2006 *Phys. Plasmas* **13** 056116
- [18] Helander P. and Simakov A.N. 2008 *Phys. Rev. Lett.* **101** 145003
- [19] Hirsch M. *et al* 2008 *Plasma Phys. Control. Fusion* **50** 053001
- [20] Ida K. *et al* 1991 *Phys. Fluids B* **3** 515
- [21] Ida K. *et al* 2001 *Phys. Rev. Lett.* **86** 5297
- [22] Ida K. and Nakajima N. 1997 *Phys. Plasmas* **4** 310
- [23] Yoshinuma M. *et al* 2009 *Nucl. Fusion* **49** 075036
- [24] Briesemeister A. *et al* 2012 Accepted for publication in *Plasma Phys. Control. Fusion* **54**
- [25] Sánchez J. *et al* 2011 *Nucl. Fusion* **51** 094022
- [26] Chmyga A. *et al* 2002 *Proc. 29th EPS Conf. (Montreux), 2002* vol 26B (ECA), p O1.09
- [27] Estrada T. *et al* 2009 *Plasma Phys. Control. Fusion* **51** 124015
- [28] Dinklage A. *et al* 2012 *to be presented in the IAEA Conf.*
- [29] Zurro B. *et al* 2006 *Fusion Sci. Technol.* **50** 419
- [30] Rapisarda D. *et al* 2005 *EPS Conf. Plasma Phys. Tarragona (Spain)*.
URL: http://epsppd.epfl.ch/Tarragona/pdf/P2_086.pdf
- [31] Velasco J.L. *et al* 2012 *Phys. Rev. Lett.* In Press
URL: <http://arxiv.org/abs/1206.1025>
- [32] Carmona J.M. *et al* 2006 *Rev. Sci. Instrum.* **77** 10F107
- [33] Hoang-Binh D. 2005 *Computer Phys. Communications (Elsevier)* **166** 191
- [34] Arévalo J. *et al* 2010 *Rev. Sci. Instrum.* **81** 10D705

- [35] Hutchinson I.H. 2002 *Principles of Plasma Diagnostics*, Cambridge University Press (2 edition)
- [36] Rapisarda D. *et al* 2007 *Plasma Phys. Control. Fusion* **49** 309
- [37] Hirshman S.P. *et al* 1986 *Phys. Fluids* **29** 2951
- [38] Velasco J.L. *et al* 2011 *Plasma Phys. Control. Fusion* **53** 115014
- [39] Velasco J.L. and Castejón F. 2012 *Plasma Phys. Control. Fusion* **54** 015005
- [40] van Milligen B. Ph. 2011 *Rev. Sci. Instrum.* **82** 073503
- [41] Guasp J. and Liniers M. 2000 *Nucl. Fusion* **40** 411